

Chapter 8

Terahertz Spectroscopy of Crystalline and Non-Crystalline Solids

Edward P. J. Parrott, Bernd M. Fischer, Lynn F. Gladden, J. Axel Zeitler and Peter U. Jepsen

Abstract Terahertz spectroscopy of crystalline and non-crystalline solids is probably one of the most active research fields within the terahertz community. Many potential applications, amongst which spectral recognition is probably one of the most prominent, have significantly stimulated the development of commercial systems and have spurred an increased technical advancement. However, the topic is very complex and multifaceted. Therefore, it is beyond the scope of this chapter to provide a fully comprehensive review of the works performed in this area. We would rather like to demonstrate, based on some selected examples, the potential the technique holds for various different applications. A particular focus will be given to data analysis and, in particular, how we may account for effects resulting from non-ideal sample preparation.

E. P. J. Parrott
Department of Electronic Engineering, The Chinese University of Hong Kong,
Hong Kong, China
e-mail: parrott@ee.cuhk.edu.hk

B. M. Fischer
Institut franco-allemand de recherches de Saint-Louis,
68301 Saint-Louis Cedex, France
e-mail: bernd.fischer@isl.eu

L. F. Gladden and J. A. Zeitler (✉)
Department of Chemical Engineering and Biotechnology,
University of Cambridge,
Cambridge CB2 3RA, UK
e-mail: jaz22@cam.ac.uk

P. U. Jepsen
DTU Fotonik-Department of Photonics Engineering,
Technical University of Denmark,
2800 Kongens Lyngby, Denmark
e-mail: puje@fotonik.dtu.dk

8.1 Introduction

Infrared spectroscopy is one of the most widely used standard techniques for characterisation and investigation of structure and composition of solid, liquid and gaseous samples. There is hardly any chemical research facility not using an infrared spectrometer, and the technique is also commonly used in industrial production sites for material characterisation and quality control. It was proposed four decades ago that the low frequency end of the far-infrared range was very well suited to investigating the material properties of solids [1–3]. However, due to constraints with regard to the available far-infrared spectrometer technology a more comprehensive investigation was delayed and the number of publications reporting the far-infrared spectra of various samples remained low. With the advent of THz-TDS in the 1990s, this changed significantly and the number of reports on spectra of chemical substances, semiconductors, organic materials and bimolecular samples continues to increase to this day.

The characteristic spectroscopic signatures, which are commonly observed in the spectra of many crystalline samples, spurred an increased interest in THz-TDS. Many possible applications based on spectral recognition of these fingerprints were proposed and soon spectral catalogues containing entries of various substances such as explosives, pharmaceuticals, food additives and biomolecules were compiled (<http://thzdb.org>). However, the potential of THz-TDS for the investigation and characterisation of solids goes well beyond spectral recognition alone. Due to the fact that this technology gives experimental access to the full dielectric function, and thus both extinction and phase information, studies of conductivity, internal structure, and impurities are just a few of many applications. Over the past two decades, the spectra of a multitude of different crystalline and non-crystalline samples have been recorded in order to investigate what additional THz-TDS studies can reveal that is not accessible with the more established technologies. In some cases, THz-TDS has indeed found its niche, a trend that is underlined by the still growing number of companies offering commercial systems. In some other cases technical as well as operational restraints still hinder a more widespread application of the technology, while very promising preliminary studies have demonstrated the proof-of-principle for further applications. Inevitably, in a small number of cases it has been shown that terahertz technologies do not appear to give additional insights into those already obtained from well-established techniques.

Given the very large number of reports of spectroscopic data of crystalline and non-crystalline solid samples, the scope of this chapter is not to provide a comprehensive review of all studies that have been performed in this area. Furthermore, our intention is not to provide a spectral data collection. Based on some selected examples, we will outline the potential of terahertz spectroscopy for identification and characterisation of various substances and highlight aspects of the measurements which require careful consideration. In particular, in order to successfully exploit the full potential of THz-TDS measurements, it is essential to understand the contributions to the spectra caused by scattering or multiple reflections. While a careful sample

preparation can minimise these contributions in laboratory-based research or forensic studies, it cannot completely avoid them. Therefore, a detailed knowledge of the phenomena that give rise to the spectral artefacts can help to improve the capabilities of THz-TDS. We will therefore outline, wherever applicable, how sample preparation and data analysis can help to enhance the quality of the recorded data in order to enhance the system performance. In many on-site industrial or security applications, however, where specific sample preparation is not practicable, atmospheric attenuation, superimposed spectroscopic features of mixtures, as well as surface and material scattering, are just some of the restraints that still need to be fully addressed. In this chapter the emphasis is thus on the potential of THz-TDS for analytical studies.

The chapter is structured as follows: in order to facilitate an understanding and interpretation of the data, several measurement considerations need to be addressed. We will briefly discuss the effect of scattering on the terahertz spectra. This is particularly important since, given a lack of well-pronounced spectroscopic features for many samples, scattering artefacts may obscure relevant information. For a more detailed coverage of scattering and scattering effects we refer to the chapter by Zurk and Schecklman. We will then consider aspects of sample preparation and extraction of the optical constants with particular focus on thin films and heterogeneous mixtures. Section 8.3 is dedicated to crystalline solids, with a focus on small organic crystalline materials. The specific signatures which are typically found in the far-infrared spectra of most organic crystalline substances enable not only spectral recognition, but also allow us to extract information about the morphology of the samples; this has led to many studies on polymorphism and phase transitions. While the spectra of non-crystalline solids show typically less pronounced and less distinct features, they can still reveal very important information about structure, conductivity, dynamics and morphology. Section 8.4 describes some latest developments in THz spectroscopy of ordered carbonaceous materials and inorganic glasses.

8.2 Measurement Considerations

8.2.1 Scattering

Scattering is discussed in more detail in Chap. 5; however, the basics are reproduced here in order to discuss their specific effects on spectroscopic measurements at terahertz frequencies.

8.2.1.1 Mie Scattering

Mie theory is derived in general terms from Maxwell's equations by considering the interaction of waves at surfaces between the scattering particle and the surrounding media, the derivation and description are outside the scope of this chapter; however,

excellent treatments are given in the following references: [4–6]. The key parameters are the Mie coefficients a_m and b_m for computing the amplitudes of the scattered field. These are written for the general case as follows:

$$a_m = \frac{n^2 j_m(nx) [x j_m(x)]' - \mu_1 j_m(x) [nx j_m(nx)]'}{n^2 j_m(nx) [x h_m^{(1)}(x)]' - h_m^{(1)}(x) [nx j_m(nx)]'} \quad (8.1)$$

$$b_m = \frac{\mu_1 j_m(nx) [x j_m(x)]' - j_m(x) [nx j_m(nx)]'}{\mu_1 j_m(nx) [x h_m^{(1)}(x)]' - h_m^{(1)}(x) [nx j_m(nx)]'} \quad (8.2)$$

where n is the relative refractive index of the sphere relative to the medium, $x = ka$ is the size parameter, a the radius of the sphere and k is the wavenumber of the electromagnetic (EM) radiation in the medium. μ_1 is the ratio of the magnetic permeability of the sphere to the magnetic permeability of the medium. This will be assumed to be 1 in the subsequent calculations. The functions $j_m(z)$ and $y_m(z)$ are spherical Bessel functions and $h_m^{(1)}(z) = j_m(z) + i y_m(z)$ are the spherical Hankel functions of order $m = (1, 2, \dots)$, with the primed versions identifying the mean derivatives with respect to the argument. As a consequence of these functions, solutions to the scattering efficiencies for a given sphere at a particular wavelength can be found as a series of terms.

Of particular interest to terahertz measurements and imaging is the Mie extinction efficiency, Q_{ext} , which is a measure of the interaction of radiation with a scattering sphere normalised to the particle cross-section, πa^2 . The extinction efficiency can be calculated from a_m and b_m in Eqs. 8.1 and 8.2 as follows [5]:

$$Q_{\text{ext}} = \frac{2}{x^2} \sum_{m=1}^{\infty} (2m+1) \Re(a_m + b_m). \quad (8.3)$$

The key outcome of the Mie theory calculation is the oscillatory behaviour of the extinction efficiency around and above wavelengths comparable to the radius of the scatterer. Figure 8.1a plots the extinction efficiency as a function of frequency (in the terahertz region) for three different scatterers with sizes ranging between 50 and 200 μ . Figure 8.1b shows the absorption coefficient spectrum for a liquid sample containing an air bubble, where a large loss feature is observed at approximately 1 THz. This feature is due to the scattering of the terahertz radiation off a spherical inclusion with approximately the same dimensions as the wavelength of the incident radiation. In this figure the Mie extinction efficiency for a sphere of radius of 150 μm is overlaid for comparison, which can be seen to contain a similar feature centred around the same frequency.

From an experimental point of view it is very important to be aware of Mie scattering when it comes to terahertz spectroscopy of solid samples as the wavelength of terahertz radiation (typically between 3 mm and 75 μm) often overlaps with the length-scale of the particle size of sample material in powder form. Wherever practical

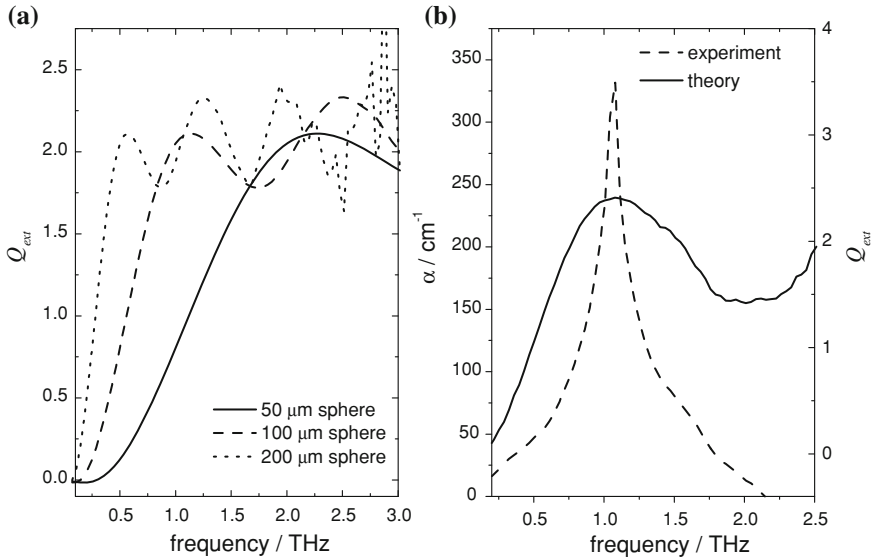


Fig. 8.1 Mie scattering. **a** Simulated Q_{ext} for three different scatterer radii, calculated using Eq. 8.3. **b** Absorption coefficient observed for a liquid sample of ethyl lactate containing a small air bubble (dashed line). The solid line is the corresponding extinction efficiency for a scatterer of a radius of 150 μm

it is advisable to mill the sample to smaller particles sizes and sieve the resulting powder to avoid scattering artefacts.

8.2.1.2 Rayleigh Scattering

Whilst the Mie scattering calculations introduced above will remain valid, it is sometimes useful to consider the analytic solution to the scattering of light due to isotropic, homogeneous and small (in comparison to the wavelength) particles, first formulated by Lord Rayleigh. Because the particle dimensions are small in comparison to the wavelength, it can be assumed that the E-field due to the incident radiation is uniform over the extent of the particle. As a result the field inside the particle (E_{int}) due to the externally varying E-field (E_{ext}) can be represented by the following relation:

$$E_{\text{int}} = \frac{3\epsilon_2}{\epsilon_1 + 2\epsilon_2} E_{\text{ext}} \quad (8.4)$$

where ϵ_1 and ϵ_2 are the permittivities of the sphere and external media respectively. Using Eq. 8.4 it can be shown that the scattering (σ_s) and absorption (σ_a) cross-sections for a spherical particle of radius a can be written as:

$$\sigma_s = \frac{8\pi}{3} k^4 a^6 \left| \frac{\epsilon_1 - \epsilon_2}{\epsilon_1 + 2\epsilon_2} \right|^2 \quad (8.5)$$

$$\sigma_a = k \frac{\Im[\epsilon_1]}{\epsilon_2} \frac{4\pi a^3}{3} \left| \frac{3\epsilon_2}{\epsilon_1 + 2\epsilon_2} \right|^2. \quad (8.6)$$

In particular, it is useful to note the fourth power dependence of the wavenumber on the scattering cross-section (Eq. 8.5). Due to the relatively long wavelengths at terahertz frequencies when compared to the particle sizes of the materials normally measured in pellet form ($<100 \mu\text{m}$), most THz-TDS measurements are undertaken in the Rayleigh scattering regime.

While in most cases, it is favourable to keep the scattering contribution to the extinction spectrum as low as possible in order to obtain a relatively good estimation of the pure absorption properties of a sample, the scattered signal can itself reveal important information about the internal structure of the substance under investigation. Png et al. [7] investigated whether THz-TDS can give an indication on the structural properties of lysozyme samples. They observed that the differences in the extinction spectra, which enabled them to differentiate between fibrillar and globular lysozyme, can be explained by Rayleigh scattering due to the morphological difference of the sample structure.

8.2.1.3 The Christiansen Effect

As we will describe in Sect. 8.2.2, one of the most commonly used sample preparation methods for polycrystalline substances is diluting the sample with a low-absorbing filler material. The mixture can then be pressed into plane-parallel pellets using a hydraulic press. The resulting pellets are mechanically stable and allow for easy handling. The ratio between filler material and sample can be optimised in order to resolve strong absorption features while at the same time avoiding saturation [8]. If the sample under investigation has a coarse grain structure, it is preferable to grind the crystals to a fine powder with grain sizes of the same order of magnitude as the filler material (typically around $100 \mu\text{m}$) to obtain a homogeneous sample and for increased mechanical stability of the pellet. In some cases, however, grinding is not practicable prior to dilution, and the spectroscopic signatures of such coarse samples typically show a characteristic scattering feature: a broadening of the low frequency wing of the absorption bands while the high frequency wing remains very sharp (see Fig. 8.2). This specific line shape (in particular the sharp drop on the high frequency side of the absorption band) cannot easily be described by Mie scattering theory.

Franz et al. have shown that the Christiansen effect, which weights the scattering of the electromagnetic radiation on the crystals by their opacity, can be employed to successfully model such scattering effects [9]. In this approach, the difference in the dielectric function of the filler material and the sample is considered. In THz-TDS, the filler material is typically polyethylene (PE), which exhibits low absorption and a nearly constant refractive index in the THz region. In most cases the refractive index

of the sample material is higher than that of PE and its slope varies significantly in the vicinity of a resonance. When the refractive indices of sample and filler intersect, the mixture appears to be homogeneous. At this frequency, the Christiansen frequency f_{Chr} [10], the scattering contribution is minimised and the sample has a maximum transparency. For other frequencies where the two refractive indices differ, the coarse sample grains have a varying degree of opacity and thus act as scattering centres. Given that the sample typically has a higher refractive index compared to the filler, the intersection usually occurs at the normal mode resonances, where the index rises at the low frequency wing of the resonant feature and drops at the higher frequency end. The opacity, and thus scattering, is therefore enhanced at the low frequency wing of the resonance while it is less pronounced at the high frequency wing.

Based on Raman's work to describe the Christiansen effect for optical light by calculating the attenuation of a wave travelling through a medium which could be divided into thin layers with different but homogeneous refractive indices [11], Franz et al. proposed a formalism to separate the scattering from the material absorption of the sample. If several material parameters such as the refractive index of both the filler and sample material together with the shape, concentration and distribution of the sample grains are known, the following equation can be used to calculate the overall absorption:

$$\alpha' = \alpha + \alpha_{\text{sc}} = \alpha + K^2 \frac{\omega^2}{c^2} (\Delta n^2) S^2, \quad (8.7)$$

where α describes the material absorption, α_{sc} the scattering contribution and Δn is the refractive index difference between sample and filler material. The parameter K describes the sample shape, average size and concentration, whereas S is a parameter describing the typical optical thickness of a thin layer of particles. Note that this formalism already requires a detailed knowledge of the material parameters in order to reproduce the characteristic line shape. Franz et al. have also shown that by assuming a flat baseline for the corrected material absorption and using Eq. 8.7 in a fit to reproduce the experimental data the parameters K and S can be determined phenomenologically.

Figure 8.2 shows the absorption coefficient α of a mixture of finely ground DL-phenylactic acid mixed with PE and pressed with a hydraulic press into a solid pellet (solid black line). The nearly flat baseline indicates that scattering artefacts can almost be neglected. The solid dots show the results for a coarse ground sample. In this case the characteristic asymmetric line shape described previously, where the vibrational modes exhibit broadening on the lower frequency side, is clearly observed. The scattering contribution due to the Christiansen effect can be calculated using the refractive index n of a pure sample or it can be derived from the mixture as described by Franz et al. [9]. The parameters K and S have been chosen such that the sum of the absorption of the finely ground sample (which can be approximated as scattering-free) and the scattering contribution match the spectrum of the coarse ground sample.

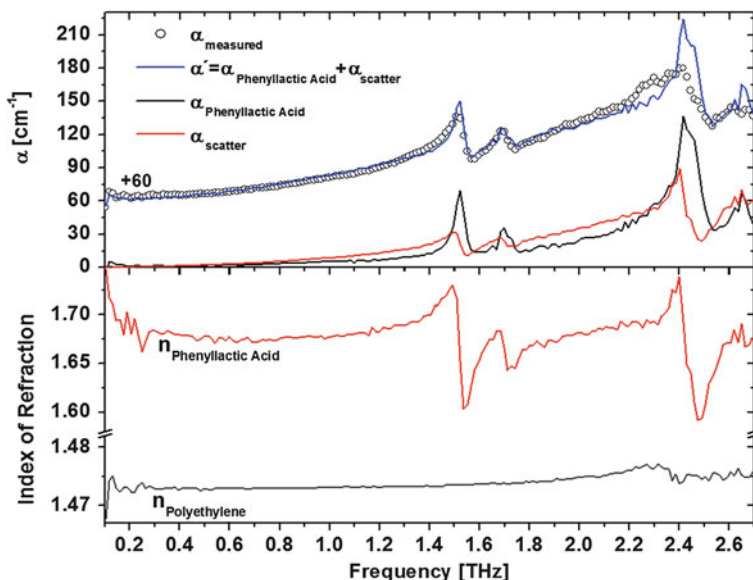


Fig. 8.2 Upper figure Absorption coefficient α of finely ground (*open dots*) and coarse ground (*solid black line*) DL-Phenylactic acid. The contribution of the scattering according to Eq. 8.7 using the refractive index depicted in the lower subfigure is shown as *solid red line*. Lower figure corresponding refractive indices. Figure adapted from [9]

8.2.2 Sample Preparation

The majority of all studies focusing on the characterisation of materials using terahertz spectroscopy is carried out in transmission geometry. This is not to say that there is not a considerable interest in reflection geometry as well, given that this sampling scheme has distinct advantages for the analysis of samples, in particular for routine sample identification in an industrial context or when dealing with strongly absorbing materials. Attenuated total reflection (ATR) in particular shows considerable potential for such applications and a number of studies have started exploring this field.

However, transmission spectroscopy is by far the most commonly used method and a transmission time-domain spectrometer is likely to be the most extensively used instrument for research groups pursuing an interest in spectroscopy. This dominance is due to the fact that it is much easier to understand the light-matter interaction in this geometry and achieve quantitative results given that the path length of the terahertz beam propagating through the sample is well-defined. However, for a fully quantitative measurement there remain a number of important considerations to be taken into account arising from the pulsed nature of the terahertz beam and the resulting complexity of the received signal due to multiple internal reflections that occur when the terahertz pulse propagates through the sample. This topic will be

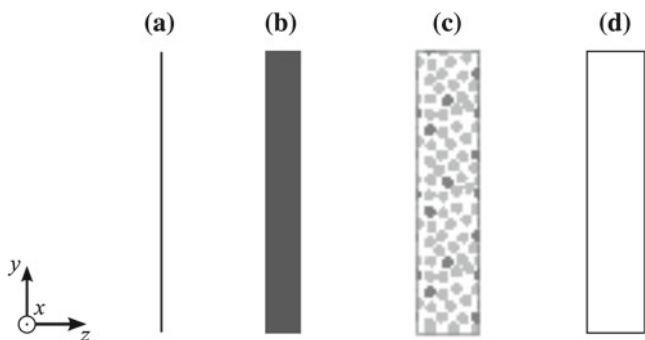


Fig. 8.3 Commonly encountered sample geometries in transmission THz-TDS (beam propagation in z -direction): **a** free standing thin film; **b** homogeneous slab of sample material; **c** porous pellet of sample particles (*dark*) and a transparent binder such as PE (*light*); and **d** thin film of sample on transparent substrate such as z -cut quartz

discussed in Sect. 8.2.3 and the reader is also referred to the chapters by Peiponen and Gornov as well as the chapter by Apostolopoulos and Daniell for a more detailed description.

When it comes to transmission spectroscopy the sample needs to be shaped to form a uniform slab of material with parallel faces in order to allow for the pulse of terahertz radiation to propagate freely through the sample and for any subsequent echo reflections to reach the detector. Sometimes, for example in the case of samples of glasses or single crystals, the sample is already a homogeneous slab of material which can be measured directly in the terahertz spectrometer (Fig. 8.3a, b); however, more frequently the sample is a powder and hence needs to be shaped into a more suitable form for terahertz analysis.

Powdered materials are typically compressed into a disc or pellet with sufficient diameter not to clip the terahertz beam at any point during the propagation through the sample and its sample holder. The beam waist at the focal point is usually in excess of 1 mm and depending on the sample thickness a diameter of 10–20 mm for the sample pellet is commonly encountered. Most materials are too strongly absorbing, show insufficient mechanical stability on direct compaction or there is insufficient material available to form a pellet of the required dimensions. In such cases a pellet is formed by dilution of the sample material with a binder which is transparent at terahertz frequencies (Fig. 8.3c).

The most popular binder for this purpose is PE which is widely available in powder form with a particle size of less than 100 μm . PE has excellent transmission properties at terahertz frequencies. It is easy to mix without sticking to surfaces, chemically inert with most solid materials, not hygroscopic and forms pellets of excellent mechanical stability. Its main disadvantage is its low melting point (which can be as low as 350 K depending on the grade of product) which makes it unsuitable for spectroscopic studies at elevated temperatures. For such experiments poly(tetrafluoroethylene) (PTFE) is a popular alternative. Although sample preparation with PTFE is a little more

difficult, due to its tendency to stick to surfaces, its melting point (around 600 K, again depending on the average molecular weight) is sufficiently high to study most organic molecules.

Alternative sample preparation techniques include casting a free-standing film for polymer materials (Fig. 8.3a) or preparing a thin film of highly absorbing materials on a transparent substrate such as z-cut crystalline quartz or silicon (Fig. 8.3d). The type of sample preparation needs to be considered when extracting the optical constants from the measured time-domain waveform to account for the different losses due to the porosity of the sample as well as the possibility of multiple internal reflections.

8.2.3 Calculation of Optical Constants

As in all other spectroscopic techniques, spectra of materials at terahertz frequencies can be acquired in either a transmission or reflection modality. For transmission mode measurements, the most common calculation directly implements the Beer–Lambert absorption formalism, however, a number of researchers have explored the use of treatments that include multiple internal reflections by involving Fresnel reflection coefficients in order to extract more accurate constants. In reflection mode, optical constants are extracted using the reflection coefficients.

In the case of spectrometers that acquire the spectra using dispersive prisms or gratings at a single frequency at a time, the measured data can be directly transformed into the frequency dependent optical constants. In THz-TDS the time-varying electric field of a terahertz pulse is measured and thus a time-domain waveform is acquired (hence the name). In order to calculate the frequency-dependent optical constants, the time-domain information must be transformed into the frequency domain using a Fourier transform. From this operation, the frequency-dependent optical properties of the sample of interest may be extracted from the broadband frequency representation of the transient. This section summarises the basic theories and equations used to calculate the optical constants from the frequency domain data.

8.2.3.1 Beer–Lambert Law

The Beer–Lambert (BL) formalism is commonly used in the extraction of optical constants from transmission measurements. The frequency-dependent refractive index $n(\nu)$ and absorption coefficient $\alpha(\nu)$ are calculated using the following equations:

$$n(\nu) = 1 + \frac{c}{2\pi\nu(\Delta x)} \{ \angle E_{\text{ref}}(\nu) - \angle E_{\text{sam}}(\nu) \} \quad (8.8)$$

$$\alpha(\nu) = \frac{2}{(\Delta x)} \ln \left\{ \left| \frac{E_{\text{ref}}(\nu)}{E_{\text{sam}}(\nu)} \right| \frac{[n(\nu) + n_{\text{med}}]^2}{4n(\nu)n_{\text{med}}} \right\}, \quad (8.9)$$

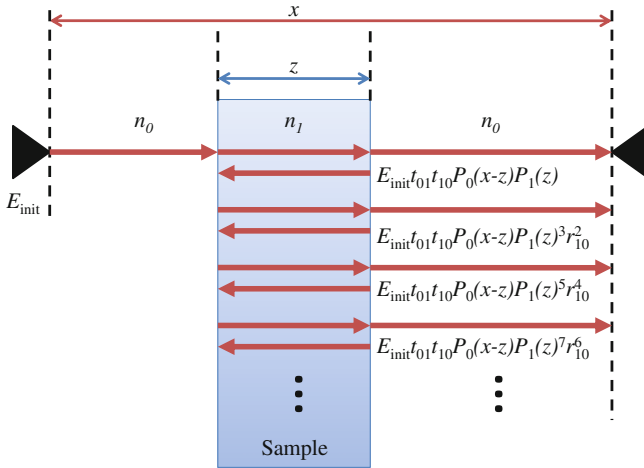


Fig. 8.4 Schematic of a basic model of the propagation of electromagnetic radiation through a sample of thickness z with refractive index n_1 and surrounding media characterised by refractive index n_0 . The terahertz pulse propagates from the source (*left* of the sample) to the detector (*right* of the sample) along x

where Δx is the thickness of the sample, n_{med} is the refractive index of the medium the sample is contained within (for example air) and E_{ref} and E_{sam} are the frequency-dependent E -fields of the terahertz transient measured for a reference and after transmission through the sample, respectively. As discussed in Sect. 8.2.2 commonly, in studies of both crystalline and non-crystalline materials the sample of interest will often be in powdered form. In these cases the sample will often be mixed with a diluent such as PE or PTFE, both of which are almost transparent to terahertz radiation, and pressed into pellets for measurement. The reference E -field, E_{ref} is then measured as the terahertz transient after propagation through a pellet of pure diluent, and containing the same mass of diluent as used in the sample pellet.

8.2.3.2 Treatment of Multiple Reflections

Every interaction of EM radiation with an interface between two materials of differing refractive indices results in the propagation of both a forward, transmitted wave and a backward, reflected wave. The amplitudes of the E -fields of the two waves are governed by the Fresnel reflection and transmission coefficients, which for a normal incident wave at the interface between regions of refractive index n_j and n_k are as follows (Fig. 8.4):

$$r_{jk} = \frac{n_j - n_k}{n_j + n_k} \quad (8.10)$$

$$t_{jk} = \frac{2n_j}{n_j + n_k}. \quad (8.11)$$

The BL formalism outlined previously considers only the first pulse to reach the detector. However, in materials with a significant refractive index mismatch with the surrounding media large subsequent reflections will occur, causing “sawtooth” or so-called “etalon” oscillations in the resultant absorption coefficient and refractive index spectra. These features can be reduced by considering the transmitted E -field as a sum of these reflected pulses [12–15]. This results in the following equation:

$$\begin{aligned} E_{\text{out}}(\nu) &= E_{\text{init}}(\nu) t_{10} t_{01} P_1(z) P_0(x - z) \\ &\quad \left(1 + P_1^2(z) r_{10}^2 + P_1^4(z) r_{10}^4 + P_1^6(z) r_{10}^6 + \dots \right) \\ &= E_{\text{init}}(\nu) t_{01} t_{10} P_1(z) P_0(x - z) \sum_{i=0}^{\delta} \left(P_1^2(z) r_{10}^2 \right)^i \end{aligned} \quad (8.12)$$

where r_{01} , t_{01} and t_{10} are Fresnel reflection and transmission coefficients as defined in Eqs. 8.10 and 8.11, x is the distance from source to detector and P_m (with $m = 0, 1, \dots$) is the material interaction term:

$$P_m(z) = \exp\left(\frac{-i2\pi\nu\tilde{n}_m z}{c_0}\right). \quad (8.13)$$

By comparing the ratio of the measured E -field after propagation through the sample and the initial E -field with the theoretical expression in Eq. 8.12 a value for the optical constants at each frequency may be found by minimising the difference in the theoretical and experimental results. This technique has been used in essentially this form in the study of semiconductors [12, 13], biomolecules [14] and inorganic glasses [16, 17].

A common modification of Eq. 8.12 is to consider an optically thin sample deposited on a much thicker substrate (Fig. 8.3d, of refractive index n_2 and thickness y) as having an infinite number of reflections. Consequently, if E_{ref} represents the E -field measured after propagation through the substrate only, then Eq. 8.12 reduces to the following form:

$$E_{\text{out}}(\nu) = E_{\text{ref}}(\nu) \frac{t_{01} t_{12} P_1(z) P_0(-z)}{t_{02} (1 + r_{01} r_{12} P_1(z)^2)}. \quad (8.14)$$

Equation 8.14 is used in the same way as described previously for the general single material case, and may be employed for both thick and thin materials. However, it is most commonly used in studies involving thin films, for example in the study of ordered carbonaceous materials [18–20, for example].

8.2.3.3 Heterogeneous Mixtures

In many situations powdered materials are embedded, compressed or coated onto a different substrate or matrix, forming a heterogeneous sample. In such situations, whilst the Beer–Lambert calculation introduced in Sect. 8.2.3.1 previously may be used, consideration of the interaction of the terahertz electric field with the heterogeneous sample will give more accurate calculations for the optical properties of the material of interest. This may be achieved by employing an effective medium approximation (EMA). The two EMAs most commonly used in the study of heterogeneous samples with terahertz radiation are attributed to Maxwell–Garnett [21] and Bruggeman [22]. Both take as a starting point the equation for the polarisability of a sphere embedded within a material of a different dielectric permittivity, α_{sp} :

$$\alpha_{\text{sp}} = 4\pi\epsilon_0 a^3 \frac{\epsilon_2 - \epsilon_1}{\epsilon_2 + 2\epsilon_1} \quad (8.15)$$

where a is the radius of the sphere and ϵ_0 , ϵ_1 and ϵ_2 are the permittivities of free space, the host dielectric and the inclusion dielectric, respectively. From Eq. 8.15 both the Maxwell–Garnett (MG) EMA and Bruggeman (BR) EMA may be derived.

Maxwell–Garnett EMA

The MG EMA may be derived from noting that the polarisability of a sphere, defined in Eq. 8.15, is proportional to its volume. Consider the example in Fig. 8.5a. In this case the polarisation of the large sphere of dielectric ϵ_{eff} (the variable to be calculated) embedded within the substrate ϵ_{sub} will just be a sum of the polarisations of the inclusions ϵ_{inc} within the sphere. Therefore:

$$\begin{aligned} \alpha_{\text{eff}} &= \sum \alpha_{\text{inc}} \\ V_{\text{eff}} \frac{\epsilon_{\text{eff}} - \epsilon_{\text{sub}}}{\epsilon_{\text{eff}} + 2\epsilon_{\text{sub}}} &= \sum_{k=1}^N V_{\text{inc},k} \frac{\epsilon_{\text{inc}} - \epsilon_{\text{sub}}}{\epsilon_{\text{inc}} + 2\epsilon_{\text{sub}}} \\ \therefore \frac{\epsilon_{\text{eff}} - \epsilon_{\text{sub}}}{\epsilon_{\text{eff}} + 2\epsilon_{\text{sub}}} &= f \frac{\epsilon_{\text{inc}} - \epsilon_{\text{sub}}}{\epsilon_{\text{inc}} + 2\epsilon_{\text{sub}}} \end{aligned} \quad (8.16)$$

where f is the volume fraction (or filling factor) of the inclusions, defined as:

$$f = \frac{\sum_{k=1}^N V_{\text{inc},k}}{V_{\text{eff}}}. \quad (8.17)$$

Equation 8.16 is the Maxwell–Garnett approximation for a single inclusion embedded within a substrate. As shown in a later paper by Maxwell–Garnett it is simple to extend this to n different types of inclusions within a substrate if one

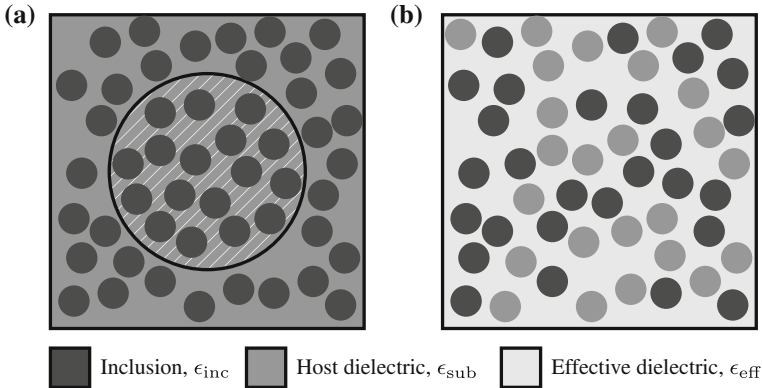


Fig. 8.5 Schematics of the respective effective medium models **a** Maxwell–Garnett (MG) dielectric model and **b** Bruggeman (BR) model

knows the volume fractions of each species of inclusion [23]. There are, however, some limitations of this technique. The most important limitation to be aware of is that this approximation will only truly hold in the limit of a fairly low volume fraction of inclusion. The reason for this is that it is implicitly assumed that there is no interaction between the inclusions as the substrate they are embedded in remains unaffected by their presence. In principle the volume fraction polarisability used above to derive Eq. 8.16 could be reduced to include just a single inclusion and the same result should be possible for any inclusion and similar size sphere. However, if the volume fraction becomes too large then the effective sphere would no longer necessarily be embedded within a homogeneous substrate. In cases where the volume fraction of the inclusion is significantly larger than that of the substrate it may be advantageous to reverse these definitions and instead consider the inclusion as the substrate and vice versa; if this is done it is commonly known as the Cavity Maxwell–Garnett model [24].

Bruggeman EMA

As illustrated in Fig. 8.5b, the set-up for the Bruggeman approximation differs somewhat from that used in the Maxwell–Garnett approximation. Instead of considering the substrate and inclusions separately they are instead both considered as inclusions, this time within a substrate that is in fact the effective dielectric material with permittivity ϵ_{eff} [22]. This elegantly removes the problem encountered by the Maxwell–Garnett model: as the “substrate” is now defined by the inclusions it is implicitly immune to any changes at high volume filling factors. For the permittivity of the substrate within Fig. 8.5b to be accurately represented by ϵ_{eff} , the total polarisability of the spherical particles within must sum to zero. Taking f to signify the volume fraction for the “inclusion” particles and therefore $1 - f$ to signify the

volume fraction for the “substrate” particles and by summing the polarisabilities of these particles the Bruggeman formula is found:

$$f \frac{\epsilon_{\text{inc}} - \epsilon_{\text{eff}}}{\epsilon_{\text{inc}} + 2\epsilon_{\text{eff}}} + (1 - f) \frac{\epsilon_{\text{sub}} - \epsilon_{\text{eff}}}{\epsilon_{\text{sub}} + 2\epsilon_{\text{eff}}} = 0 \quad (8.18)$$

8.2.4 Dynamic Range

In THz-TDS the dynamic range varies greatly with frequency. As discussed in Chap. 1 by Freeman et al. typically the signal-to-noise range in the frequency spectrum that is calculated from the terahertz pulse reaches a maximum just below 1 THz and then drops off exponentially towards higher frequencies until it reaches the noise level (Fig. 8.6). Depending on the characteristics of the emitter/detector devices and the laser used the signal drops to the noise level at the cut-off frequency ν_{max} , which is typically anywhere between 1 and 4 THz, although the spectral bandwidth in some spectrometers can extend up to 7 THz (e.g. by using GaP for detection [25]) or even beyond [26].¹

The dynamic range of a THz-TDS measurement will therefore vary both from instrument to instrument and from sample to sample. Following from Eq. 8.9 Jepsen and Fischer [27] have shown that the maximum absorption that can be measured reliably at a given dynamic range (DR) is

$$\alpha(\nu)_{\text{max}} \Delta x = 2 \ln \left[\text{DR} \frac{4n(\nu)}{(n(\nu) + 1)^2} \right]. \quad (8.19)$$

Here, we assume that n_{med} from Eq. 8.9 is unity, i.e. that the measurement is acquired in a dry nitrogen or vacuum atmosphere. Whenever $\alpha(\nu)_{\text{max}}$ is exceeded the spectrum will not drop to the noise level immediately but rather exhibit an apparent absorption coefficient of α_{max} , which steadily decreases until it reaches zero at ν_{max} .

In the case of a narrow absorption peak exceeding the dynamic range the peak is clipped and its peak shape changes completely. This makes it stand out from the other peaks and it is obvious that the resulting peak is dominated by the artefact. However, the absorption spectra that are acquired from materials which are strongly absorbing over a wide range of frequencies can be much more misleading at first sight. Materials such as polymers or inorganic crystals typically show very broad absorption features or a monotonous increase in absorption up to the frequency where α_{max} is reached. In such cases misinterpretations of the spectra from this frequency to ν_{max} are possible as the resulting spectrum often resembles a broad, albeit somewhat noisy, peak (Fig. 8.6).

In order to measure a good quality terahertz spectrum using THz-TDS it is therefore important to carefully consider the particle size, the amount of sample material,

¹ Useable bandwidths in excess of 20 THz have been reported by using terahertz radiation generated in a plasma. A detailed explanation of how this can be achieved is provided in Chap. 14 by Hoffmann.

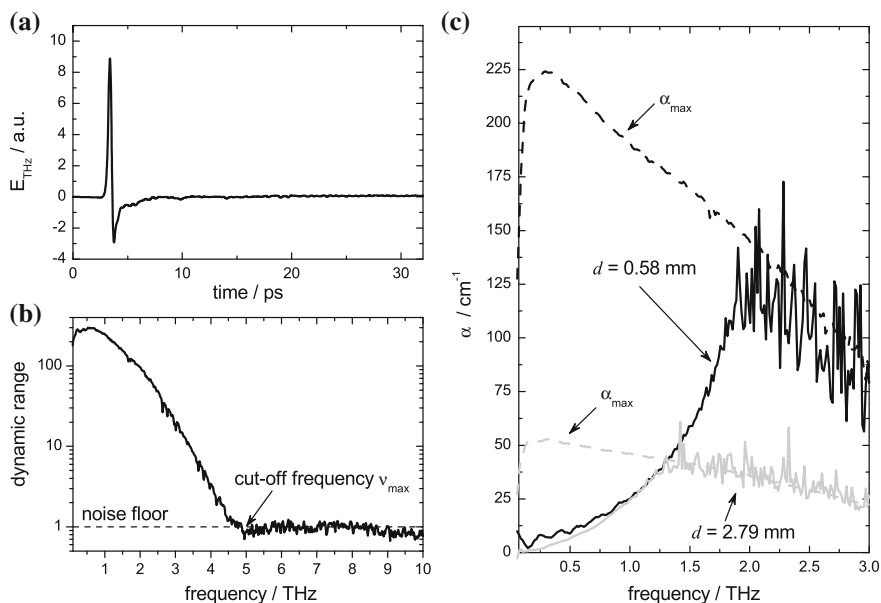


Fig. 8.6 Terahertz pulse **a** and corresponding power spectrum **b**. The cut-off frequency ν_{max} is defined as the frequency at which the signal drops to the noise floor. Absorption spectrum of two samples of poly lactide with different thicknesses **c**. The dashed line marks the maximum dynamic range that can be achieved in this measurement. Figure **c** modified from [27]

the method of sample preparation as well as the most suitable parameter extraction algorithm. In practise there is often a trade-off between spectral resolution, bandwidth and absolute error in the optical constants and it can be necessary to prepare multiple samples of different relative sample concentrations to achieve both a high spectral bandwidth as well as good confidence in the absolute values of α and n .

8.3 Spectroscopy of Crystalline Solids

In this section we will give an overview of how terahertz radiation can be used to study the structure and dynamics of a range of materials. Here, we will focus on crystalline materials while the following section will provide an insight into the type of spectra that can be acquired from non-crystalline materials. A particular focus of this section will be on crystalline samples of small organic molecules.

As outlined in Chap. 7 by Tomerini and Day, terahertz spectroscopy is a very sensitive technique to probe the interaction of crystalline phonons as well as the *intermolecular* hydrogen bonds in small organic molecular crystals. The vibrational modes that can be observed at terahertz frequencies represent the collective motions of the atoms corresponding to translations and librations of the molecules in the unit

cell, and terahertz spectra of this class of materials have been found to be very rich in spectral signatures at terahertz frequencies.

8.3.1 Biomolecules

The first examples using THz-TDS to study biomolecules were reported by Markelz et al. [28] as well as by Walther et al. [29]. Markelz measured the terahertz absorption of lyophilized powders of calf thymus DNA, bovine serum albumin (BSA) and collagen using THz-TDS. The results showed that all three molecules exhibit a broadband terahertz response with no distinct vibrational modes, which was attributed to a large density of low frequency modes. However, it was observed that the broadband response was different between molecules. A conformational change was proposed as a mechanism which may preferentially excite one or some of these low frequency modes, resulting in an observed change in the absorption spectrum. Later research confirmed that terahertz spectroscopy is sensitive to conformational changes, since clear changes in the terahertz spectrum of bacteriorhodopsin were observed upon illumination by light, which is known to cause a change in the conformational state of the biomolecule [30].

Walther and coworkers attempted to differentiate three isomers of retinal: all-*trans*, 13-*cis* and 9-*cis* versions, taking measurements in the solid state at both room (298 K) and low (10 K) temperatures [29]. The low temperature spectra were successfully fitted using a Lorentz oscillator model [31], and by comparing the terahertz spectra of the three isomers the same feature, that was reported at 54 cm^{-1} for all three isomers, was tentatively assigned to an intramolecular vibrational mode of the carbon ring, which is unchanged between the three isomers. This study represented one of the first investigations into the assignment of vibrational features at terahertz frequencies, an area of research that has now matured into a rapidly burgeoning field of its own and is discussed in-depth in the previous chapter by Tomerini and Day. However, whilst crystalline materials, in particular pharmaceutical compounds and explosives, have been at the forefront of the refinement of mode assignment routines, biomolecules have not. This can be explained by the large size and complexity of the biomolecules and as a result, the normal mode distributions, which dominate the terahertz absorbance, are similar for various biomolecules.

Subsequent measurements using THz-TDS have been reported for the various nucleobases and nucleosides (i.e. nucleobases with a deoxyribose sugar molecule attached) of DNA [32]. In two further studies, dry powders of both sulphur-containing biomolecules and sulphur-peptide dimers were investigated using THz-TDS [33] and THz-TDS and Raman spectroscopy [34]. Differences observed in the recorded terahertz spectra for these various biomolecules were attributed in each case to changes in the inter- and intramolecular bonding.

The study of biomolecules in the solid state represented an important step in the evolution of THz-TDS as an analytic technique with applications beyond the specialist laser laboratory. It demonstrated that vibrational spectroscopy at frequen-

cies below what was previously accessible by far-infrared techniques provided exciting new opportunities to characterise relatively similar large molecules by probing their intermolecular and low-frequency intramolecular modes. The results suggested that THz-TDS has a unique sensitivity to intermolecular interactions with many potential applications in chemistry and biology. With more groups becoming active in the field in the following years the focus in terahertz spectroscopy of biomolecules moved away from solid-state spectroscopy towards investigating peptides and proteins in solution (see next chapter by George and Markelz).

More recently, THz-TDS of solids has focussed on investigating much smaller, and hence potentially less complex molecules, in order to better understand the origin of the vibrational modes that are observed at terahertz frequencies. Small organic molecular crystals were found to be a fruitful field of research as the intermolecular interactions between the molecules fall right into the terahertz range. Within this class of materials research into the properties of pharmaceutical drug molecules and explosive materials at terahertz frequencies has been a particular focus of activity.

8.3.2 *Small Organic Molecules*

8.3.2.1 Solid-State Chemistry

The ability to perform non-invasive chemical recognition of materials using THz-TDS has long been proposed as a significant and useful application of the technique. Studies of the terahertz spectra of benzoic acid and its derivatives, and also of glucose, fructose and sucrose demonstrated that chemically similar crystalline materials exhibit very different terahertz signatures due to their different molecular crystal structures [35, 36]. Later studies broadened the range of materials studied to include drugs of abuse such as cocaine and morphine, as well as lactose monohydrate, acetylsalicylic acid, sucrose and tartaric acid (Fig. 8.7a) [37].

Ranitidine hydrochloride was one of the first pharmaceutical drug molecules that was studied using THz-TDS in an investigation by Taday et al. at Teraview, a company involved in the commercialisation of terahertz radiation based in Cambridge, UK [38]. The initial rationale was that pharmaceutical solids had long been known to exist in more than one crystalline form and that such distinct forms, or polymorphs, have the same chemical formula but different crystalline structures that can lead to different physical and chemical properties for the material. Such differences in crystal structure, which are reflected in different lattice energies of the resulting crystals, can impact the pharmaceutical performance of the drug by changes in the rate of drug dissolution and ultimately influence the bioavailability of the drug. Given that terahertz radiation is sensitive to longer range vibrational modes set up within a crystal structure, it seemed likely that THz-TDS was well placed to distinguish between such polymorphs. Indeed, this has been found to be that case.

While it is possible to detect changes in crystal structure between polymorphs by X-ray diffraction experiments, such measurements are typically destructive and

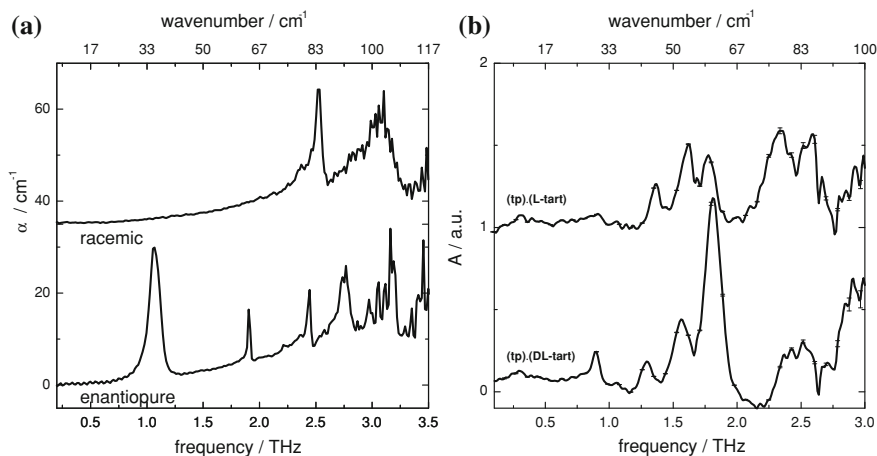


Fig. 8.7 **a** Terahertz spectra of the racemic and enantiopure forms of tartaric acid (Figure modified from [37]); **b** spectra of cocrystals formed between theophylline and both the racemic and enantiopure forms of tartaric acid (Figure modified from [39])

therefore cannot be performed on the final tablet. In 2003, there were effectively no quick and convenient methods for confirming the polymorphic state of the drug while in storage, and so the authors investigated whether THz-TDS could perform this role. Two forms of ranitidine hydrochloride were investigated and they displayed a clear difference in their terahertz absorption across the frequency range, demonstrating that THz-TDS is sensitive to changes in the intermolecular interactions due to alterations to the intermolecular crystalline form.

This finding has generated much interest in the pharmaceutical and analytical chemistry communities as it demonstrated a clear advantage of THz-TDS over any other vibrational spectroscopy techniques. While it is straightforward to differentiate different molecules using infrared or Raman spectroscopy based on the distinct vibrational modes associated with the functional groups present in the molecules, terahertz spectroscopy was found to be more sensitive to the intermolecular interactions between molecules in a crystal and hence it was able to differentiate between different solid-state modifications.

Differences in the terahertz spectra have been reported between polymorphic forms of the pharmaceutical materials carbamazepine (form I and III), enalapril maleate (form I and II), indomethacin (crystalline and amorphous forms) and fenoprofen calcium (crystalline and liquid crystalline forms) [40], furosemide [41] and manitol [42] among others and it is now widely accepted that THz-TDS is an excellent fingerprinting technique to identify different polymorphs of organic molecular crystals.

Two studies that serve as a good example to illustrate the sensitivity of the technique are the investigation of sulfathiazole which has at least five polymorphs all of which were easily identified using THz-TDS but not with Raman or mid-infrared

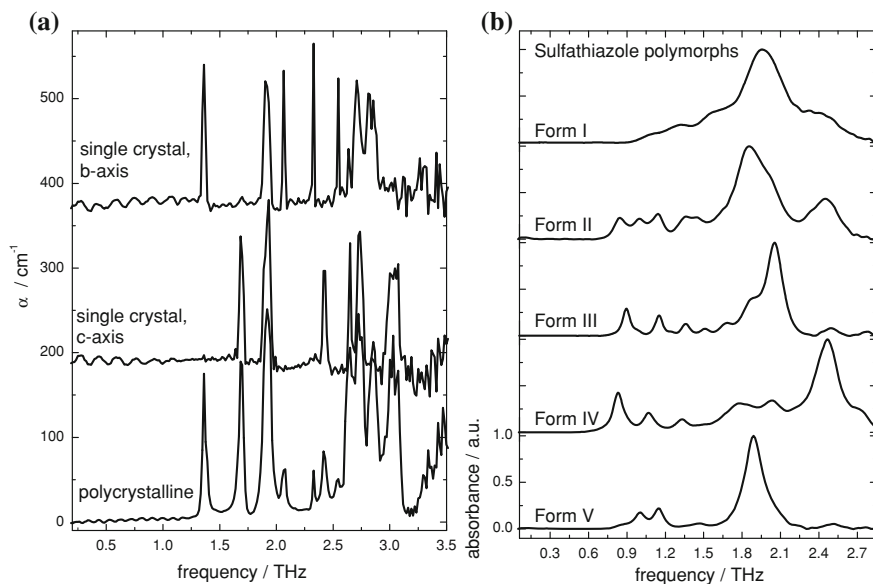


Fig. 8.8 **a** Terahertz spectra of polycrystalline sucrose as well as spectra from a single crystal depending on its orientation to the terahertz beam (unpublished data by Fischer et al.); **b** Terahertz spectra of the five known polymorphs of sulfathiazole. The samples only differ in the crystal packing of the sulfathiazole molecules, the molecules are chemically identical. (Figure modified from [43])

spectroscopy [43] (Fig. 8.8), as well as the straightforward identification of a set of cocrystals [39] that only differs in the stereochemistry of one of the cocrystal formers and appears isostructural in standard X-ray diffraction and Raman spectroscopy analysis.

8.3.2.2 Chemical Imaging

In analogy to near-infrared and Raman imaging it was possible to produce accurate chemical maps by transmission mapping of a set of seemingly identical material pellets that was made using different chemicals by selecting specific vibrational frequencies of the respective terahertz spectra [37].

In addition, chemical mapping has also been demonstrated in reflection mode. This technique is particularly powerful when resolving information at depth from a sample using techniques such as windowed Fourier transforms [44]. Based on this approach Shen et al. were able to demonstrate that it is possible to identify a material buried at depth within a larger pellet based upon the oscillations observed in the terahertz waveform at a second interface, i.e. the buried structure.

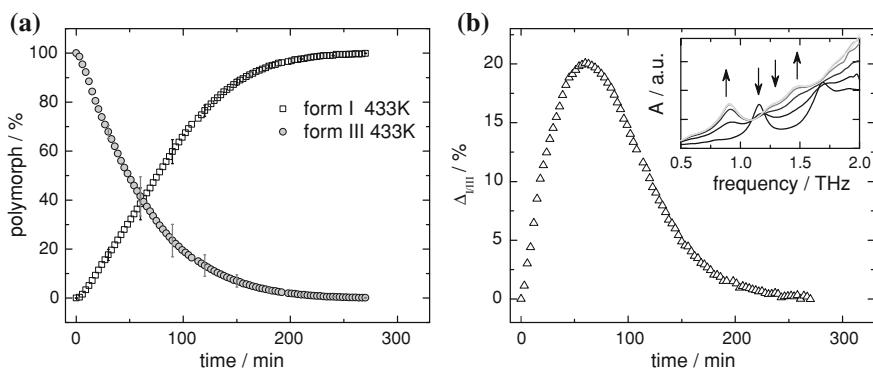


Fig. 8.9 Conversion of carbamazepine form III to I at 433 K. For clarity not all error bars are shown. **a** The decrease in Form III and subsequent formation of Form I follow different kinetics. **b** Amount of carbamazepine in the gas phase during the conversion process. The insert shows the absorption spectra of the sample during the conversion process with *arrows* indicating the associated spectral changes during the phase transition (Figure modified from [46])

8.3.2.3 Phase Transformations

A significant fraction of more recent work on pharmaceutical materials spectroscopy has focused on monitoring in situ phase transformations. For example, the phase transformation of different polymorphic forms of carbamazepine with temperature was monitored using terahertz spectroscopy [45, 46]. It was found that a clear change in the terahertz absorption spectrum could be followed as the temperature was changed. In a later study this process was analysed quantitatively and evidence was found for different rates of formation and loss for the two carbamazepine forms (as shown in Fig. 8.9). The results confirmed that the mechanism of the phase change was mediated via a sublimation step—this agreed with Differential Scanning Calorimetry (DSC) measurements and physical evidence of sublimation during the experiment but had gone previously unnoticed in two earlier studies using Raman spectroscopy and XRPD.

THz-TDS has also been used to successfully follow the temperature-induced phase transformations in sufathiazole [43], DL-cysteine [47], and theophylline [48]; in [48] it was shown that by studying the evolution of the terahertz absorption spectra, the mechanisms of the phase transformations may be elucidated. In addition to crystalline temperature transformations, amorphous to crystalline transitions [49] and dehydration processes [50] have been studied using THz-TDS. In particular, careful analysis of the amorphous to crystalline transition resulted in the identification of seven distinct material phases during the crystallisation of carbamazepine, whereas the evolution of the hydrate terahertz spectra of theophylline monohydrate revealed spectral features that are attributed to evaporating hydrate water as well as an overall evolution from the hydrate to anhydrous terahertz spectrum [50]. Evidence of evaporating hydrate water is not always observed in THz-TDS investigations of hydration

transitions, however, as in a similar study of caffeine hydrate dehydration, only the solid-state phase transformation was observed [51].

THz-TDS has been used to fit kinetic models to time-resolved dehydration reactions [52]. In this case a time resolved dehydration reaction of D-glucose monohydrate has been monitored at various temperatures, in order to investigate the kinetics of the reaction. By monitoring the evolution of a spectral feature, the normalised dehydration fraction was quantified for each spectrum recorded. These data were then fitted to numerous kinetic models and it was found that the two-phase boundary-controlled reaction equation best described the observed kinetics for all reaction temperatures investigated. THz-TDS was therefore able to suggest both a plausible reaction mechanism and to calculate an activation energy for the dehydration reaction (149 kJ mol^{-1}).

THz-TDS has also been used to follow the reaction of benzoquinone and dihydroxybenzene to form quinhydrone, a 1:1 complex stabilised by hydrogen bonds. This reaction has been observed to occur spontaneously, and the reaction mechanism confirmed by monitoring the terahertz spectra and comparing them to spectra of the initial species and quinhydrone formed from solution [53]. Monitoring the formation of products using THz-TDS has also been attempted on the formation of cocrystals via mechano-grinding [54]. The reactants were chosen to be featureless in the terahertz region, whereas the cocrystal product was known to have some strong spectral features, allowing the researchers to follow the growth of this feature during the reaction. The terahertz results appear to suggest the presence of an amorphous phase in the ground cocrystals.

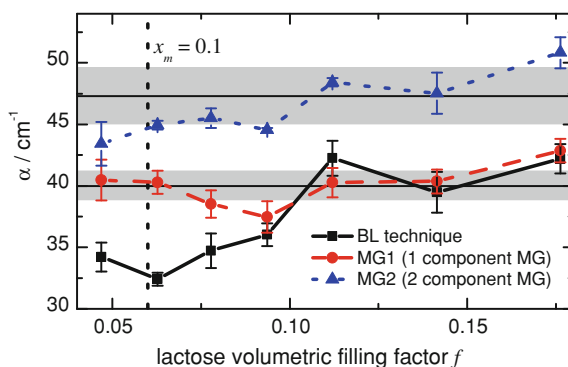
Monitoring phase transitions, and where possible extracting information about the kinetics of these transitions in situ represent an exciting use for THz-TDS in the future.

8.3.2.4 Analytical Applications

In order to quantify the amount of a particular pharmaceutical material within a sample, researchers have investigated the potential of chemometrics using multivariate data analysis such as Partial Least Squares (PLS) methods [55]. By using PLS methods it is possible to extract the percentage of a material within these compound samples by considering the absorption spectrum of the tablet recorded using THz-TDS and comparing this to the pure sample spectra. PLS methods have been employed to accurately predict the percentage concentration of two forms polymorphic forms within a pellet [56], and also to chemically map pellets formed of lactose and sucrose [57]. Given sufficiently different spectral features, the accuracy of the THz-TDS PLS techniques have been found to be comparable to or exceeding other commonly used approaches [55, 56].

Mixtures of solid chemical materials have been used to test the analytic capabilities of THz-TDS. Mixtures of isomers of benzoic acid have been measured using THz-TDS and by assuming a simple mixing rule and knowledge of the individual chemical

Fig. 8.10 Comparison of the peak height calculated for the lactose absorption feature in a PE/lactose composite pellet at 0.56 THz using either the BL law (*black squares*), a one-component MG model (*red dots*) or a two-component MG model (*blue triangles*). The corresponding values extracted from pure lactose pellets are shown as the grey bands. Data taken from Ref. [59]



spectra it was possible to accurately predict the concentrations of the various isomers within the mixture, with a total analytical error of about 6% [58].

Effective medium approximations (EMAs) have also been used to further improve the accuracy of extracted optical constants [59]. Using the Maxwell–Garnett [21] approximation outlined in Sect. 8.2.3.3 it is possible to extract consistent optical constants for lactose α -monohydrate embedded in a PE matrix at various filling factors, which agreed with the data for pellets of pure lactose. By contrast, conventional mixing techniques tended to underestimate the optical constants at low filling factors (as shown in Fig. 8.10).

By extending the technique to include a second inclusion (air), the contribution to the dielectric properties of the pellet due to the air could also be included. A drawback to this technique, however, is that the Maxwell–Garnett model assumes spherical inclusions, and often inclusions will not be of a uniform shape. Tuononen advocates the use of Wiener bounds to constrain the value of the dielectric constant of an inclusion given a known filling fraction [60]. This simple treatment yields the maximum and minimum possible values for the dielectric constants and assumes nothing regarding the shape of the inclusions; however, if small changes are to be monitored the changes are likely to be within the upper and lower bounds. Consequently, Scheller and coworkers have advocated an extension to the Maxwell–Garnett model purporting to account for all the limitations of that model [61]. Their formulation can account for ellipsoidal inclusions of varying shapes and sizes and can cope with high filling factors.

8.3.2.5 Beyond the Pellet

The experiments described above have all prepared the samples in a similar fashion—taking powdered samples and pressing them into pellets, commonly after mixing with a diluent such as PE. Melinger and Grischowsky have pioneered an alternative preparation technique based on waveguides [62, 63], and have used waveguide THz-TDS to study pharmaceutical materials, as well as other chemicals and explosives.

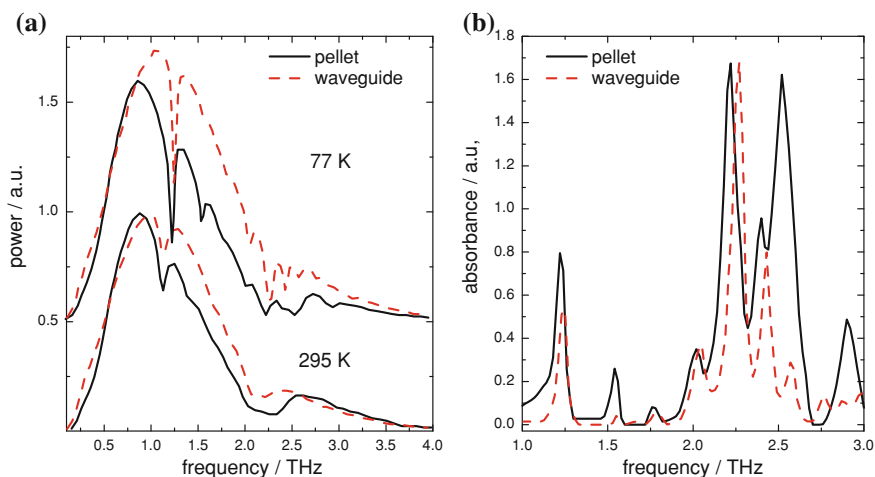


Fig. 8.11 **a** Power spectra for salicylic acid extracted either from a pellet or from a thin film desposited on a waveguide at both 295 K and 77 K; **b** the corresponding absorbances calculated for the pellet and waveguide techniques at 77 K. Data reproduced from Ref. [64]

Laman et al. studied acetylsalicylic acid and its precursors using waveguide THz-TDS and compared these results with conventional THz-TDS using pellets [64]. Figure 8.11 shows a comparison of the power spectra and absorption spectra measured for salicylic acid either through a pellet or using a waveguide film. It is found that whilst similar vibrational frequencies are recorded for the vibrational modes, both the relative intensities and the degree of broadening reported were very different for the two techniques. Broadening can be classified as either homogeneous or inhomogeneous. Homogeneous broadening typically shows a distinct temperature dependence, whereas inhomogeneous broadening is relatively insensitive to temperature. Both the pellet and waveguide THz-TDS spectra display prominent line-narrowing upon cooling, suggesting homogeneous broadening dominates. However, the degree of narrowing at low temperatures is much higher in the waveguide THz-TDS spectra, thereby increasing the ability to distinguish distinct vibrational modes when using this form of sample preparation.

It should be highlighted, however, that waveguide THz-TDS and pellet THz-TDS will not necessarily produce comparable spectra, due to the highly preferred orientation that the thin films grown on the waveguides can exhibit when compared to the pellets. During film deposition the molecules tend to form oriented thin films. As a result, the THz-TDS will couple to vibrational modes within the molecule to a different extent in the film and pressed pellet samples. In addition, there can be some interfacial disorder in pellet samples, which can lead to a shift in the baseline due to the amorphous content, depending on how the sample powder was prepared. This becomes particularly significant when milling the sample material for prolonged periods to achieve a smaller particle size. Clearly, care needs to be taken when

comparing data recorded using the waveguide THz-TDS with traditional pellet THz-TDS.

It is also important to note that the waveguide approach will be limited when looking at different polymorphs or solid-state modifications of a material given that it will be very difficult, if not impossible, to crystallise all different forms selectively on the waveguide surface.

8.3.3 Explosives

Due to the security implications of being able to detect and measure explosive materials, the potential uses of THz-TDS in detecting and understanding explosives has been widely investigated since an initial investigation of the potential security applications of terahertz radiation [65] and the dedicated study of trinitro-s-triazine [66] as well as dinitrotoluene [67]. The research interests have followed two broad themes: identification (with a specific aim of eventual stand-off detection) and interpretation of spectral features using computer simulation.

8.3.3.1 Identification

Trinitrotoluene (TNT), Research Department Explosive (RDX), cyclotetramethylene-tetranitramine (HMX) and pentaerythritol tetranitrate (PETN) have been the explosives of choice for THz-TDS studies. The terahertz spectra of TNT, RDX and PETN mixed with PE and pressed into pellets have been measured up to 6 THz using a thin GaP detector, almost doubling the measured spectral range of these materials [68]. Clearly, increasing bandwidth is advantageous in order to further discriminate between different chemical species. Single crystal samples of HMX, RDX and PETN have also been measured using THz-TDS [69]. Numerous dependencies have been observed in the spectra of these materials based on the orientation of the crystal, suggesting that in the future, if single crystals are available they may help constrain and understand the origin of the vibrational modes. Waveguide THz-TDS has been used to study the spectra of explosives such as TNT and RDX [70]. The extremely low sample amounts required for waveguide THz-TDS (in this case $\approx 150 \mu\text{g}$ is required for the RDX spectrum) is often cited as a significant advantage for this technique, as the amount of explosive material is typically 1 % of the sample mass required for a typical sample pellet. Waveguide THz-TDS produces extremely sharp spectral lines, especially at low temperatures, when compared to similar measurements of pellets, and this, combined with the extremely low sample amounts required, offers a safe and reliable technique for identifying suspect powders.

Clearly, in the security environment, stand-off detection is required (or at the very least preferred) for a technique to be useful. The terahertz spectra of 17 explosives and related compounds measured using THz-TDS have been compiled, including the ability of THz-TDS to reliably identify explosives in transmission mode that were

placed behind 1 mm thick covering materials such as plastic and leather [71]. It has been found that it is still possible to clearly identify the unique fingerprint for the explosives even when concealed within a common cover material; a useful further step would be to investigate the same capability in reflection mode, as this is likely to be the most useful measurement geometry in practice. The terahertz spectrum of RDX has been measured in reflection mode (without any concealing layers) and it was found that it was possible to observe differences between lactose, sucrose and RDX [72].

8.3.3.2 Computer Simulation of Spectral Features

The evolution of the techniques and abilities of computational programming packages to identify and understand crystalline materials is studied in-depth in Chap. 7; however, it is important to note the importance of the study of explosive materials with THz-TDS to this particular field. Explosive compounds represent one of the most widely studied families of crystalline materials with regard to systematic evaluation of the various commercially available density functional theory (DFT) techniques. The DMol³ DFT package has been evaluated in the study of the spectra of PETN, β -HMX and RDX and compared with experimental data [73–75]. PETN has also been studied using different DFT packages, CASTEP and PWscf [76], as has HMX using the plane wave code ab init [77]. These studies focused more upon the computational variables within these calculations, but highlight the scientific importance of the explosive compounds in driving the evolution and development of these computational techniques.

8.3.4 Other Crystalline Materials

The characteristic signatures, which dominate the spectra of organic molecular crystals, have received particular attention due to the potential for specific applications described above. However, they represent only one class of crystalline materials. Indeed, terahertz spectra of semiconductors had been investigated well before the first reports on terahertz spectroscopic studies of organic crystals appeared [78]. Pigments and similar materials have recently been studied by many research groups, as they are potentially relevant to the investigation of paintings and similar works of art. THz imaging has proven to be a very useful tool for revealing previously undiscovered information in the study of layered paintings [79]. Another vast and still growing research field is dedicated to the spectroscopic investigation of ceramics. The list of materials which are currently investigated by THz spectroscopy could certainly be extended, and to give a complete picture is far beyond the scope of this chapter. We therefore would like to refer the interested reader to the detailed description of some of these aspects in Chap. 10 by Johnson and Lloyd-Hughes, and Chap. 21 by Fukunaga and Picollo.

8.4 Spectroscopy of Non-Crystalline Solids

8.4.1 Glasses

An amorphous solid such as a glass is one with a structure which lacks periodicity, extended symmetry and long-range order. As such the characterisation of these materials presents very different challenges to the crystalline materials investigated in Sect. 8.3, as the absence of periodicity removes the sharp spectral features associated with crystalline materials. However, whilst they are isotropic at long length scales, X-ray diffraction measurements have revealed quasi-crystalline arrangements on local (atomic and molecular) scales [80]. Vibrational anomalies in glasses were initially noticed from measurements of the low temperature heat capacities of silica [81], where a clear departure from the vibrational behaviour predicted by Debye theory ($C_p \propto T^3$) was observed. Specifically, a peak in the density of states is observed, with the maximum usually occurring around 1 THz [80]. This peak is commonly called the boson peak. This behaviour appears to be specific to glasses, and is thought to relate to the disorder of the material. Therefore THz-TDS, as a method to probe the frequency range of interest for these features arising from structural disorder, would appear to be a useful tool in understanding the structure and dynamics of glasses, despite the lack of sharp spectral features. Whilst this section focuses on the work that has been performed in order to characterise inorganic glasses, terahertz spectroscopy has also been used to study amorphous organics [36, 40, 49], such as the polymer characterisation discussed in Chap. 13 by Jansen et al.

8.4.1.1 Inorganic Glasses

One of the first spectroscopic measurements using THz-TDS reported in the literature was a study incorporating amorphous materials, such as silica [78]. For this study, a large disc of silica was produced with a diameter of 50 mm and thickness of 6.449 mm in order to maximise the interaction length. This was possible due to the very low terahertz absorption characteristics and allowed a very precise measurement of the low frequency absorption coefficient to be extracted. For comparison studies on materials with larger absorption coefficients such a thick sample would be impractical. Additionally, it is often difficult to produce more exotic samples with such volumes and preserve homogeneity. More recently, studies using THz-TDS of commercially available glasses, which are usually mixtures of different amorphous solids (e.g. SiO_2 , B_2O_3 , Na_2O and Al_2O_3) [82], and SiO_2 and arsenic sulphide (As_2S_3) [83], have been reported.

8.4.1.2 Interpreting the Terahertz Optical Constants

Taraskin et al. [83] proposed a universal frequency dependence for the relationship between the vibrational density of states (VDOS) and the infrared absorption coefficient, for frequencies below that of the boson peak which is of the following form:

$$\alpha(\omega) = C(\omega)g(\omega) \simeq (A + B\omega^2)g(\omega) \quad (8.20)$$

where A and B were material-dependent constants relating to the degree of uncorrelated and correlated charge fluctuations, respectively. In particular, the uncorrelated charge fluctuation coefficient A is related to the variance of the uncorrelated charge distribution σ_1^2 by the following expression:

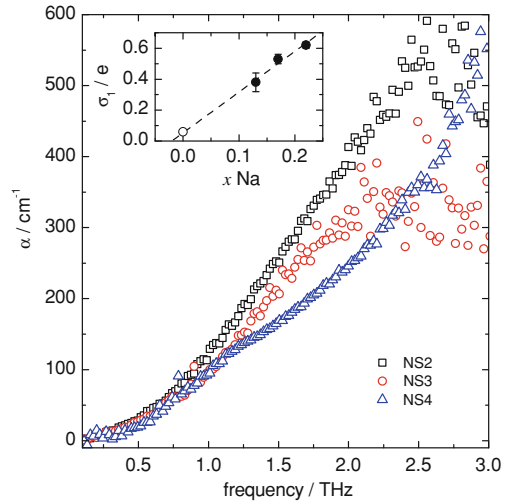
$$\sigma_1^2 = \frac{A\bar{m}c_0\sqrt{\epsilon_\infty}}{2\pi^2n} \quad (8.21)$$

where \bar{m} , ϵ_∞ and n are the average atomic mass, the high frequency limit of the ionic dielectric constant, and the atomic concentration respectively (c_0 is the speed of light in a vacuum). In their work, values for the infrared coupling coefficient for As_2S_3 and SiO_2 were extracted, and the results for SiO_2 agreed with the results obtained using hyper-Raman spectroscopy (HRS) [84], i.e. that the infrared coupling is proportional to the VDOS due to the low value of the B coefficient. Reference [82] found that the inclusion of additional components of the SiO_2 structure, greatly altered the terahertz absorption. Using a Debye-like model for the VDOS, they observed a frequency dependence that was approximately quadratic within the low frequency region (below 1 THz).

8.4.1.3 Further Improvements: Extraction of Accurate Optical Properties

Clearly, the accurate extraction of optical properties of these materials is of importance in order to calculate the coupling coefficient, determine the position of the boson peak and compare the infrared absorption results with other characterisation techniques. All previous studies of the far-infrared absorption in glasses used the information from the first pulse only and neglected information contained in subsequent reflections. In the case of the work by [78], due to the long interaction length the loss of information was relatively low; however, in more highly absorbing materials such as those investigated in the later experiments [82, 83], the use of thin samples limits the time domain due to internal reflections appearing much earlier in time. In materials where the terahertz absorption is high, consideration of the multiple reflections is required to extract a higher resolved measurement of the optical constants, which can be implemented by following the treatment outlined in Sect. 8.2.3.2. Such a multiple reflection extraction algorithm has been recently implemented in the study of amorphous glasses [16, 17]. In particular, it was possible

Fig. 8.12 Absorption coefficients for three sodosilicate glasses, NS x (Na $_2$ O \cdot x SiO $_2$, $x = 2,3,4$), between 0.1–3 THz. Inset: distribution of uncorrelated charges σ_1 as a function of sodium mole fraction (*closed circles*). σ_1 for pure SiO $_2$ from Ref. [83] is shown as a *open circle*



to extract accurate low frequency data of highly absorbing sodosilicate glasses, the absorption coefficients of which are plotted in the main figure of Fig. 8.12. Using Eq. 8.21 the distribution of uncorrelated charges for the three sodosilicate glasses was extracted, and an approximately linear correlation with the mole fraction of sodium observed (see the inset in Fig. 8.12), suggesting that the uncorrelated charge fluctuations are dominated by the spatial disorder of the position of the sodium atoms. Such a result was only possible by the acquisition of accurate, low frequency data.

8.4.2 Ordered Carbonaceous Materials

The first use of THz-TDS to study carbon nanotubes (CNTs) was reported by [85] in 2002. In this paper the change in optical properties upon purification of the single-walled CNTs (i.e. removal of the non-nanotube carbonaceous particles and transition metals used in the production) from the pristine (i.e. as produced) CNTs was investigated. The purified samples displayed an increased absorption coefficient and real refractive index across the frequency range investigated (in this case between 0.1 and 0.8 THz). The conductivity can be calculated by the following equation:

$$\epsilon = \epsilon_{\infty} + i \frac{\sigma}{\omega \epsilon_0}. \quad (8.22)$$

An increased absorption coefficient and real refractive index is therefore seen to result in an increased conductivity, which the authors attribute mainly to the increased crystallinity of the purified samples. The group of Jeon, in Korea, remain active in the field of terahertz studies of CNTs with further papers published in 2004 [86],

2005 [18, 87] and 2007 [88, 89]. Reference [86] presented the first use of the Drude–Lorentz (DL) model and Maxwell–Garnett (MG) Effective Medium Approximation (EMA) with THz-TDS measurements. These approaches are used to characterise the structural and electronic properties of these materials; a brief outline of the DL model is now given.

8.4.2.1 The Drude–Lorentz Model

The DL model treats the frequency-dependent dielectric constant ($\epsilon(\omega)$) as a contribution from free and bound oscillators calculated in a classical fashion. This results in the following equation for the frequency-dependent dielectric constant ($\epsilon_{\text{CNT}}(\omega)$):

$$\epsilon_{\text{CNT}} = \epsilon_{\infty} - \frac{\Omega_p^2}{\omega^2 + i\Gamma\omega} + \sum_{j=1}^{\delta} \frac{\Omega_{p,j}^2}{\omega_{0,j}^2 - \omega^2 - i\Gamma_j\omega}, \quad (8.23)$$

where Ω_p and Γ are the Drude plasma frequency and damping rate, and $\Omega_{p,j}$, $\omega_{0,j}$ and Γ_j are the Lorentz oscillator strength, oscillator frequency and damping rate for the j th Lorentz oscillator. The oscillator strength and damping rates may be represented as follows:

$$\Omega_p = \sqrt{\frac{Ne^2}{m\epsilon_0}} \quad (8.24)$$

and

$$\Gamma = \frac{1}{\tau} = Nv\sigma \quad (8.25)$$

where N is the electron density, e is the electric charge, m is the oscillator mass and v is the electron drift velocity. In the case of the Drude oscillator strength and damping rate, these parameters relate to the free, or valence, electrons, whereas for the Lorentz counterparts the parameters refer to the bound electrons.

8.4.2.2 Characterisation of Carbon Materials

The MG EMA (as defined in Sect. 8.2.3.3) needs to be used due to the preparation technique employed to prepare the CNT samples. In Ref. [86], the CNT samples were prepared into a thin film deposited on a silicon window. As a result, the terahertz beam propagates through a matrix formed of both air and CNT, thereby requiring the use of the EMA. Jeon reported that a simple Drude model was not a good fit to their CNT results; a Lorentz mode was required suggesting a combination of metallic and semiconducting nanotubes were present. Later work from Jeon and coworkers focused on the effect of functionalisation of the nanotubes with either hydrogen [87, 88] or fluorine [18], and the observed differences between single-walled and

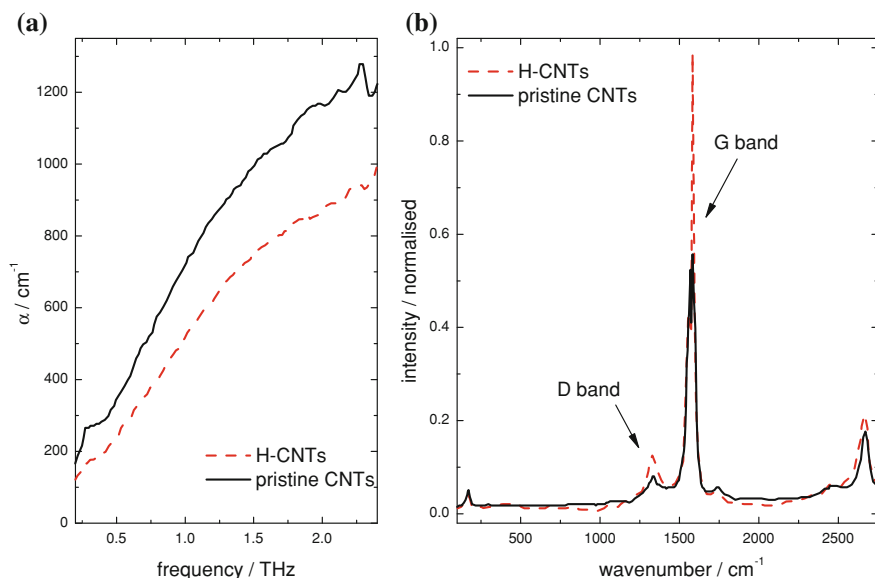


Fig. 8.13 **a** Absorption coefficient between 0 and 2.5 THz for H-CNTs (*dashed line*) and pristine CNTs (*solid line*) **b** Raman spectra for H-CNTs (*dashed line*) and pristine CNTs (*solid line*). The D and G features are highlighted

double-walled CNTs [89]. Kang et al. observed a decrease in the terahertz absorption and real refractive index upon hydrogen functionalisation of CNTs [87]. Using the DL model and the MG EMA they observed a decrease in the free electron carrier density and attributed this to the change in bonding from an sp^2 to an sp^3 bonding regime. This study was continued in Ref. [88] by including Raman spectroscopy, and the terahertz results are displayed along with the Raman spectra in Fig. 8.13. An increase in the I_D/I_G ratio was observed upon hydrogen functionalisation, which is indicative of an increase in sp^3 bonding.

Whilst Jeon and coworkers in Korea have been the most prolific researchers in the characterisation of CNTs, there have been other groups working on this challenge with terahertz spectroscopy. Federici and coworkers in New Jersey, USA performed visible pump-probe terahertz spectroscopy to investigate localised transport in Lorentz-type photoinduced states [90]. As with previous methods, they utilised a (modified) DL model to explain the terahertz transmission properties through the photoexcited layer. Researchers in Japan have also investigated CNTs with THz-TDS. Iwasa and coworkers used THz-TDS to investigate the dielectric properties of aligned CNTs between 0.1 THz and over 300 THz [91]. Large differences between the absorption properties were observed below 30 THz for nanotubes aligned parallel and perpendicular to the E -field orientation. Here, they explain some of the observed differences in terms of how the MG model is formulated to fit the data. Alignment of the CNTs means that the spherical approximation used in the basic

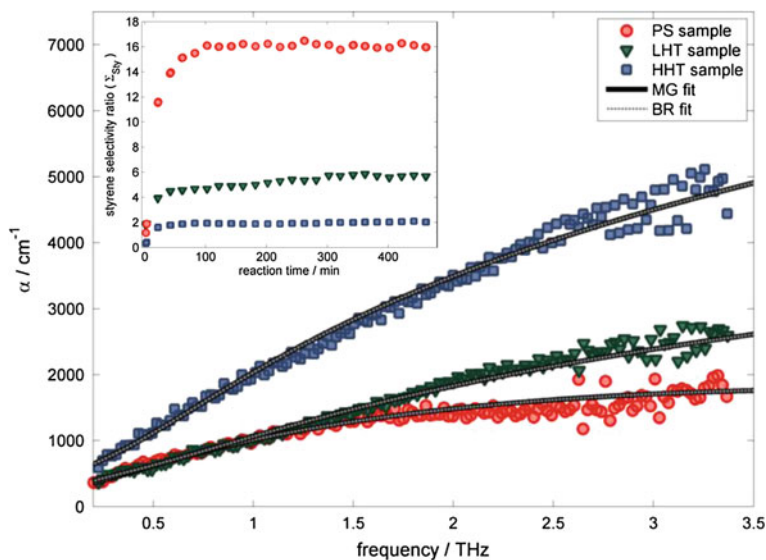


Fig. 8.14 Absorption coefficient for the three types of CNF studied in Ref. [19]. Insert: catalytic activity test results for the three CNF materials

MG model is no longer applicable and so in the limit of zero cross-section in the polarisation direction the MG model then approximates to a simple mixing model. Shimano and coworkers in Tokyo measured the dielectric properties of SWCNTs from 0.1 to 20 THz through optical rectification in a ZnTe crystal [92]. As with previous investigations, they analysed the terahertz absorption spectrum by using a DL model. With some similarities to Ref. [91], Rungsawang et al. investigated the terahertz absorption of rubber containing embedded CNTs and found that by deforming the material (stretching), alignment of the CNT could be induced and measured with THz-TDS [93]. Recently, THz-TDS has been used in order to understand and quantify differences between similar carbon nanofibres (CNFs) and CNTs [19, 20]. The definition of the difference between CNFs and CNTs is somewhat difficult to define, but commonly a CNT is defined as a carbon material exhibiting a cylindrical nanostructure with an inner diameter less than 10 nm and a CNF differs in having an inner diameter ranging between 10 and 100 nm. In the first study [19] the catalytic activity of heat-treated CNF materials was quantified using THz-TDS. Three CNF samples, identical except for their heat-treatment temperature, displayed very different catalytic activity for the dehydrogenation reaction of butane to styrene, as shown in Fig. 8.14. As can be seen in Fig. 8.14, THz-TDS is able to clearly differentiate between the three different CNFs. Using the DL model and EMAs, the observed increase in terahertz absorption with increasing heat-treatment temperature could be replicated, and attributed to an increase in the free electron density.

In a similar fashion, the degree of graphitic order in two commercially available multi-walled CNTs (Baytubes and Nanocyl) was quantified using THz-TDS and

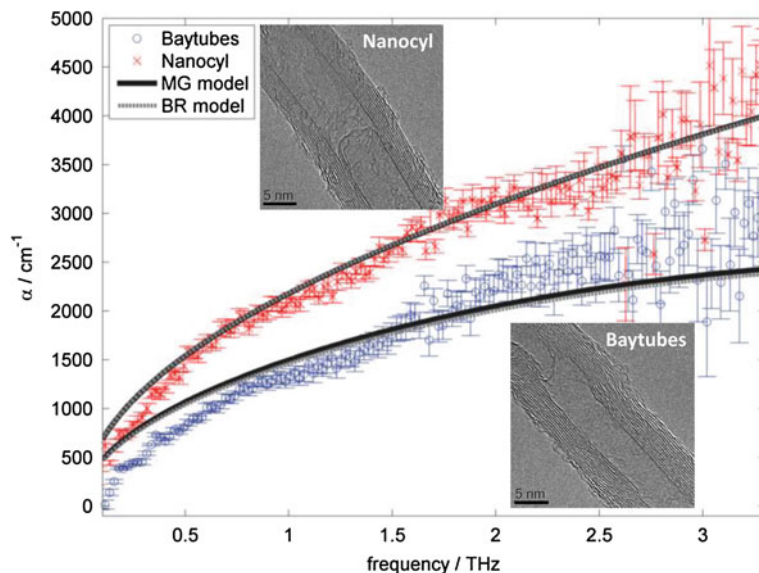


Fig. 8.15 Absorption coefficients for the two nominally similar MWCNTs studied in Ref. [20]. Inserts: Representative HRTEM images of the two MWCNTs highlighting the different graphicity of the two materials

compared to high resolution transmission electron microscopy (HRTEM) images representative of the two samples. The absorption coefficients extracted for the CNTs and the corresponding HRTEM images are shown in Fig. 8.15. The THz-TDS absorption coefficient data showed an increase across the frequency region for the Nanocyl sample when compared to the Baytubes sample, and as before use of the DL model and EMAs suggested that this change could be attributed to an increase in the free electron density in the Nanocyl CNTs. It therefore follows that a larger number of electrons are present in a delocalised bonding regime, which would be consistent with a decrease in the number of defects within the Baytubes CNTs. This correlates with the HRTEM images, where the Baytubes can be seen to display a greater number of terminations and defects in comparison to the Nanocyl sample. The results presented in all of these papers have shown the sensitivity that THz-TDS displays towards the electron density present within CNTs, and therefore by extension other forms of ordered carbon materials, such as graphene and graphite. Whilst previous studies have focused on differences between CNTs such as functionalisation, in the future it would be interesting to develop and probe the extent to which THz-TDS is directly sensitive to defect density by introducing defects into a material in a controllable manner.

In addition, the research papers reported herein used a variety of different preparation and extraction techniques in order to produce the frequency-dependent optical constants for a range of carbonaceous materials. These range from embedding the CNTs in rubber [93], mixing them with a diluent such as KBr [89] to depositing them

in a thin film on a second surface such as silicon [18, 85–88] or quartz [19, 20]. In order to be able to draw conclusions relating to the different materials investigated, it would be important to study the effects of sample preparation on the extracted optical constants and the resulting effect, if any, this would have on the fitting parameters of the DL model used to infer some explanation as to their relative properties.

8.5 Summary

Terahertz spectroscopy of crystalline and non-crystalline solids has developed into one of the largest research fields within the terahertz scientific community. Spectroscopic studies ranging across condensed matter physics, chemical physics, physical chemistry, materials chemistry, pharmaceutical sciences, chemical engineering to the food and paper industries have been reported. In addition to the shear range of activities this field of terahertz technology is also the area which has attracted most attention so far above and beyond the direct interest within the terahertz community. Some of the first materials that were investigated using terahertz spectroscopy methods were semiconductors, but it was in particular the spectra of explosives and drug molecules, which were shown to exhibit pronounced spectroscopic signatures that highlighted the potential for the wider community for this new spectroscopy technique. It was this interest that was the driving force behind the development of the first commercial terahertz systems. However, the initial surge in interest also led to some exaggerated expectations as to how the characteristic spectral features could be used for applications, in particular in the security sector. The field has matured considerably over the past few years and more realistic research-oriented studies once again dominate the community. In this chapter, based on selected examples, we have shown that the applications of terahertz time-domain spectroscopy for investigating the dielectric properties of a given material go far beyond plain spectral recognition. In order to fully exploit these capabilities it is absolutely paramount to combine careful sample preparation with more sophisticated data analysis. Given the complexity of the research topics covered in the community as well as the dynamic nature of the field, the list of data analysis approaches that we present in this chapter must not be considered exhaustive. We would like to refer the interested reader to the other chapters in this book, that cover some of these concepts in more depth.

References

1. G.W. Chantry, *Submillimetre Spectroscopy—A Guide to the Theoretical and Experimental Physics of the Far Infrared Radiation* (Academic Press, New York, 1971)
2. K.D. Möller, W.G. Rothschild, *Far-Infrared Spectroscopy* (Wiley, New York, 1971)
3. E.V. Loewenstein, D.R. Smith, R.L. Morgan, *Appl. Opt.* **12**(2), 398 (1973)
4. M. Kerker, *The scattering of light, and other electromagnetic radiation* (Academic Press, New York, 1969)

5. H.C. van de Hulst, *Light scattering by small particles* (Dover Publications, New York, 1981)
6. C.F. Bohren, D.R. Huffman, *Absorption and scattering of light by small particles* (Wiley, New York, 1983)
7. G.M. Png, R.J. Falconer, B.M. Fischer, H.A. Zakaria, S.P. Mickan, A.P.J. Middelberg, D. Abbott, *Opt. Express* **17**(15), 13102 (2009)
8. W. Withayachumnankul, B.M. Fischer, D. Abbott, *Opt. Express* **16**(10), 7382 (2008)
9. M. Franz, B.M. Fischer, M. Walther, *Appl. Phys. Lett.* **92**(2), 021107 (2008)
10. R. Barnes, L. Bonner, *Phys. Rev.* **49**(10), 732 (1936)
11. C.V. Raman, *Proc. Indian Acad. Sci. A* **29**, 381 (1949)
12. L. Duvillearet, F. Garet, J.L. Coutaz, *Appl. Opt.* **38**(2), 409 (1999)
13. T.D. Dorney, R.G. Baraniuk, D.M. Mittleman, *J. Opt. Soc. Am. A* **18**(7), 1562 (2001)
14. I. Pupeza, R. Wilk, M. Koch, *Opt. Express* **15**(7), 4335 (2007)
15. R. Wilk, I. Pupeza, R. Cernat, M. Koch, *IEEE J. Sel. Top. Quant.* **14**(2), 392 (2008)
16. E.P.J. Parrott, J.A. Zeitler, L.F. Gladden, S.N. Taraskin, S.R. Elliott, *J. Non-Cryst. Solids* **355**(37–42), 1824 (2009)
17. E.P.J. Parrott, J.A. Zeitler, G. Simon, B. Hehlen, L.F. Gladden, S.N. Taraskin, S.R. Elliott, *Phys. Rev. B* **82**(14), 140203 (2010)
18. T.I. Jeon, J.H. Son, K.H. An, Y.H. Lee, Y.S. Lee, *J. Appl. Phys.* **98**(3), 034316 (2005)
19. E.P.J. Parrott, J.A. Zeitler, J. McGregor, S.P. Oei, H.E. Unalan, S.C. Tan, W.I. Milne, J.P. Tessonnier, R. Schlögl, L.F. Gladden, *J. Phys. Chem. C* **113**, 10554 (2009)
20. E.P.J. Parrott, J.A. Zeitler, J. McGregor, S.P. Oei, H.E. Unalan, W.I. Milne, J.P. Tessonnier, D.S. Su, R. Schlögl, L.F. Gladden, *Adv. Mater.* **21**(38–39), 3953 (2009)
21. J.C.M. Garnett, *Philos. T. R. Soc. Lond.* **203**(1), 385 (1904)
22. D.A.G. Bruggeman, *Ann. Phys.* **416**, 636 (1935)
23. J.C.M. Garnett, *Philos. T. R. Soc. Lond.* **205**(1), 237 (1906)
24. J.E. Spanier, I.P. Herman, *Phys. Rev. B* **61**(15), 10437 (2000)
25. W. Fan, A. Burnett, P. Upadhyaya, J. Cunningham, E. Linfield, A. Davies, *Appl. Spectrosc.* **61**(6), 638 (2007)
26. Y.C. Shen, P.C. Upadhyaya, E. Linfield, H. Beere, A. Davies, *Appl. Phys. Lett.* **83**(15), 3117 (2003)
27. P.U. Jepsen, B. Fischer, *Opt. Lett.* **30**(1), 29 (2005)
28. A. Markelz, A. Roitberg, E. Heilweil, *Chem. Phys. Lett.* **320**(1–2), 42 (2000)
29. M. Walther, B. Fischer, M. Schall, H. Helm, P.U. Jepsen, *Chem. Phys. Lett.* **332**(3–4), 389 (2000)
30. A.G. Markelz, S. Whitmire, J.R. Hillebrecht, R. Birge, *Phys. Med. Biol.* **47**, 3797 (2002)
31. H.A. Lorentz, in *Proceedings of the KNAW*, vol. 18, p. 134, 1915
32. B.M. Fischer, M. Walther, P.U. Jepsen, *Phys. Med. Biol.* **47**(21), 3807 (2002)
33. K. Yamamoto, M.H. Kabir, K. Tominaga, *J. Opt. Soc. Am. B* **22**(11), 2417 (2005)
34. N. Brandt, A. Chikishev, A. Kargovsky, M. Nazarov, O. Parashchuk, D. Sapozhnikov, I. Smirnova, A. Shkurinov, N. Sumbatyan, *Vib. Spectrosc.* **47**(1), 53 (2008)
35. M. Walther, P. Plochocka, B. Fischer, H. Helm, P.U. Jepsen, *Biopolymers* **67**(4–5), 310 (2002)
36. M. Walther, B.M. Fischer, P.U. Jepsen, *Chem. Phys.* **288**(2–3), 261 (2003)
37. B. Fischer, M. Hoffmann, H. Helm, G. Modjesch, P.U. Jepsen, *Semicond. Sci. Tech.* **20**(7), S246 (2005)
38. P.F. Taday, I.V. Bradley, D.D. Arnone, M. Pepper, *J. Pharm. Sci.* **92**(4), 831 (2003)
39. E.P.J. Parrott, J.A. Zeitler, T. Friscic, M. Pepper, W. Jones, G.M. Day, L.F. Gladden, *Cryst. Growth Des.* **9**(3), 1452 (2009)
40. C.J. Strachan, T. Rades, D.A. Newnham, K.C. Gordon, M. Pepper, P.F. Taday, *Chem. Phys. Lett.* **390**(1–3), 20 (2004)
41. M. Ge, G. Liu, S. Ma, W. Wang, *Bull. Korean Chem. Soc.* **30**(10), 2265 (2009)
42. R. Chakkittakandy, J.A.W.M. Corver, P.C.M. Planken, *J. Pharm. Sci.* **99**(2), 932 (2010)
43. J.A. Zeitler, D.A. Newnham, P.F. Taday, T.L. Threlfall, R.W. Lancaster, R.W. Berg, C.J. Strachan, M. Pepper, K.C. Gordon, T. Rades, *J. Pharm. Sci.* **95**, 2486 (2006)
44. Y.C. Shen, P.F. Taday, *IEEE J. Sel. Top. Quant.* **14**(2), 407 (2008)

45. J.A. Zeitler, D.A. Newnham, P.F. Taday, C.J. Strachan, M. Pepper, K.C. Gordon, T. Rades, *Thermochim. Acta* **436**(1–2), 71 (2005)
46. J.A. Zeitler, P.F. Taday, K.C. Gordon, M. Pepper, T. Rades, *Chem. Phys. Chem.* **8**, 1924 (2007)
47. M. Franz, B.M. Fischer, M. Walther, *J. Mol. Struct.* **1006**(1–3), 34 (2011)
48. P. Upadhyaya, K. Nguyen, Y. Shen, J. Obradovic, K. Fukushige, R. Griffiths, L. Gladden, A. Davies, E. Linfield, *Spectrosc. Lett.* **39**(3), 215 (2006)
49. J.A. Zeitler, P.F. Taday, M. Pepper, T. Rades, *J. Pharm. Sci.* **96**, 2703 (2007)
50. J.A. Zeitler, K. Kogermann, J. Rantanen, T. Rades, P.F. Taday, M. Pepper, J. Aaltonen, C.J. Strachan, *Int. J. Pharm.* **334**(1–2), 78 (2007)
51. H.b. Liu, Y. Chen, X.C. Zhang, *J. Pharm. Sci.* **96**(4), 927 (2007)
52. H. Liu, X.C. Zhang, *Chem. Phys. Lett.* **429**(1–3), 229 (2006)
53. M. Ge, W. Wang, H. Zhao, Z. Zhang, X. Yu, W. Li, *Chem. Phys. Lett.* **444**(4–6), 355 (2007)
54. K.L. Nguyen, T. Frisčić, G.M. Day, L.F. Gladden, W. Jones, *Nat. Mater.* **6**(3), 206 (2007)
55. P.F. Taday, *Philos. T. Roy. Soc. A* **362**(1815), 351 (2004)
56. C.J. Strachan, P.F. Taday, D.A. Newnham, K.C. Gordon, J.A. Zeitler, M. Pepper, T. Rades, *J. Pharm. Sci.* **94**(4), 837 (2005)
57. Y. Shen, P. Taday, D. Newnham, M. Pepper, *Semicond. Sci. Tech.* **20**(7), 254 (2005)
58. Z. Zeng-Yan, J. Te, Y. Xiao-Han, X. Ti-Qiao, X. Hong-Jie, *Chinese Phys. Lett.* **23**(8), 2239 (2006)
59. E.P.J. Parrott, J.A. Zeitler, L.F. Gladden, *Opt. Lett.* **34**(23), 3722 (2009)
60. H. Tuononen, K. Fukunaga, M. Kuosmanen, J. Ketolainen, K.E. Peiponen, *Appl. Spectrosc.* **64**(1), 127 (2010)
61. M. Scheller, S. Wietzke, C. Jansen, M. Koch, *J. Phys. D: Appl. Phys.* **42**(6), 065415 (2009)
62. G. Gallot, S. Jamison, R. McGowan, D. Grischkowsky, *J. Opt. Soc. Am. B* **17**(5), 851 (2000)
63. J.S. Melinger, N. Laman, S.S. Harsha, D. Grischkowsky, *Appl. Phys. Lett.* **89**(25), 251110 (2006)
64. N. Laman, S.S. Harsha, D. Grischkowsky, *Appl. Spectrosc.* **62**(3), 319 (2008)
65. M.C. Kemp, P.F. Taday, B.E. Cole, J.A. Cluff, A.J. Fitzgerald, W.R. Tribe, *Proc. SPIE* **5070**, 44 (2003)
66. F. Huang, B. Schulkin, H. Altan, J.F. Federici, D. Gary, R. Barat, D. Zimdars, M. Chen, D.B. Tanner, *Appl. Phys. Lett.* **85**(23), 5535 (2004)
67. Y. Chen, H. Liu, Y. Deng, D. Schauki, M.J. Fitch, R. Osiander, C. Dodson, J.B. Spicer, M. Shur, X.C. Zhang, *Chem. Phys. Lett.* **400**(4–6), 357 (2004)
68. W.H. Fan, A. Burnett, P.C. Upadhyaya, J. Cunningham, E.H. Linfield, A.G. Davies, *Appl. Spectrosc.* **61**(6), 638 (2007)
69. J. Barber, D.E. Hooks, D.J. Funk, R.D. Averitt, A.J. Taylor, D. Babikov, *J. Phys. Chem. A* **109**(15), 3501 (2005)
70. J.S. Melinger, N. Laman, D. Grischkowsky, *Appl. Phys. Lett.* **93**(1), 011102 (2008)
71. J. Chen, Y. Chen, H. Zhao, G.J. Bastiaans, X.C. Zhang, *Opt. Express* **15**(19), 12060 (2007)
72. Y.C. Shen, T. Lo, P.F. Taday, B.E. Cole, W.R. Tribe, M.C. Kemp, *Appl. Phys. Lett.* **86**(24), 241116 (2005)
73. D.G. Allis, T.M. Korter, *Chem. Phys. Chem.* **7**(11), 2398 (2006)
74. D.G. Allis, D.A. Prokhorova, T.M. Korter, *J. Phys. Chem. A* **110**(5), 1951 (2006)
75. D.G. Allis, J.A. Zeitler, P.F. Taday, T.M. Korter, *Chem. Phys. Lett.* **463**, 84 (2008)
76. A.D. Burnett, J. Kendrick, J.E. Cunningham, M.D. Hargreaves, T. Munshi, H.G.M. Edwards, E.H. Linfield, A.G. Davies, *Chem. Phys. Chem.* **11**(2), 368 (2010)
77. C.T. Konek, B.P. Mason, J.P. Hooper, C.A. Stoltz, J. Wilkinson, *Chem. Phys. Lett.* **489**(1–3), 48 (2010)
78. D. Grischkowsky, S. Keiding, M. van Exter, C. Fattinger, *J. Opt. Soc. Am. B* **7**(10), 20062015 (1990)
79. A.J.L. Adam, P.C.M. Planken, S. Meloni, J. Dik, *Opt. Express* **17**(5), 3407 (2009)
80. E. Courtens, M. Foret, B. Hehlen, R. Vacher, *Solid State Commun.* **117**(3), 187 (2001)
81. R. Zeller, R. Pohl, *Phys. Rev. B* **4**(6), 2029 (1971)
82. M. Naftaly, R. Miles, *J. Non-Cryst. Solids* **351**(40–42), 3341 (2005)

83. S.N. Taraskin, S.I. Simdyankin, S.R. Elliott, J.R. Neilson, T. Lo, *Phys. Rev. Lett.* **97**(5), 1 (2006)
84. B. Hehlen, E. Courtens, R. Vacher, A. Yamanaka, M. Kataoka, K. Inoue, *Phys. Rev. Lett.* **84**(23), 5355 (2000)
85. T.I. Jeon, K.J. Kim, C. Kang, S.J. Oh, J.H. Son, K.H. An, D.J. Bae, Y.H. Lee, *Appl. Phys. Lett.* **80**(18), 3403 (2002)
86. T.I. Jeon, K.J. Kim, C. Kang, I.H. Maeng, J.H. Son, K.H. An, J.Y. Lee, Y.H. Lee, *J. Appl. Phys.* **95**, 5736 (2004)
87. C. Kang, I.H. Maeng, S.J. Oh, J.H. Son, T.I. Jeon, K.H. An, S.C. Lim, Y.H. Lee, *Appl. Phys. Lett.* **87**(4), 041908 (2005)
88. C. Kang, I.H. Maeng, S.J. Oh, S.C. Lim, K.H. An, Y.H. Lee, J.H. Son, *Phys. Rev. B* **75**(8), 1 (2007)
89. I. Maeng, C. Kang, S.J. Oh, J.H. Son, K.H. An, Y.H. Lee, *Appl. Phys. Lett.* **90**(5), 051914 (2007)
90. H. Altan, F. Huang, J.F. Federici, A. Lan, H. Grebel, *J. Appl. Phys.* **96**(11), 6685 (2004)
91. N. Akima, Y. Iwasa, S. Brown, A.M. Barbour, J. Cao, J. Musfeldt, H. Matsui, N. Toyota, M. Shiraishi, H. Shimoda, O. Zhou, *Adv. Mater.* **18**(9), 1166 (2006)
92. H. Nishimura, N. Minami, R. Shimano, *Appl. Phys. Lett.* **91**(1), 011108 (2007)
93. R. Rungsawang, V.G. Geethamma, E.P.J. Parrott, D.A. Ritchie, E.M. Terentjev, *J. Appl. Phys.* **103**(12), 123503 (2008)